Inorganic Chemistry

Article

pubs.acs.org/IC

A Combined Spectroscopic and Computational Study of a High-Spin $S = 7/2$ Diiron Complex with a Short Iron–Iron Bond

Christopher M. Zall,[†,§] Danylo Zherebetskyy,[†,§] Allison L. Dzubak,[†] Eckhard Bill,*[,‡] Laura Gagliardi,*[,†] and Connie C. Lu*[,†]

[†]Department of Chemistry, Superconducting Institute, and Center for Metals in Biocatalysis, University of Minnesota, 207 Pleasant Street SE, Minneapolis, Minnesota 55455-0431, United States

[‡]Max Planck Institut für Bioanorganische Chemie, Stiftstrasse 34–36, D-45470 Mülheim an der Ruhr, Germany

Supporting Information

ABSTRACT: The nature of the iron–iron bond in the mixed-valent diiron tris(diphenylforamidinate) complex $Fe_2(DPhF)_3$, which was first reported by Cotton, Murillo et al. (*Inorg. Chim. Acta* **1994**, *219*, 7–10), has been examined using additional spectroscopic and theoretical methods. It is shown that the coupling between the two iron centers is strongly ferromagnetic, giving rise to an octet spin ground state. On the basis of Mössbauer spectroscopy, the two iron centers, formally mixed-valent Fe(II)Fe(I), are completely equivalent with an isomer shift $\delta = 0.65$ mm s^{-1} and quadrupole splitting $\Delta E_Q = +0.32$ mm s^{-1}. A large, positive zero-field splitting $D_{7/2} = 8.2$ cm^{-1} has been determined from magnetic susceptibility measurements. Multiconfigurational quantum studies of the complete molecule $Fe_2(DPhF)_3$ found one dominant configuration $(\sigma)^2(\pi)^4(\pi^*)^2(\sigma^*)^1(\delta)^2(\delta^*)^2$, which accounts for 73% of the ground-state wave function. By considering all the configurations, an estimated metal–metal bond order of 1.15 has been calculated. Finally, $Fe_2(DPhF)_3$ exhibits weak electronic absorptions in the visible and near-infrared regions, which are assigned as d–d transitions from the doubly occupied metal–metal π molecular orbital to half-occupied π^*, δ, and δ^* orbitals.

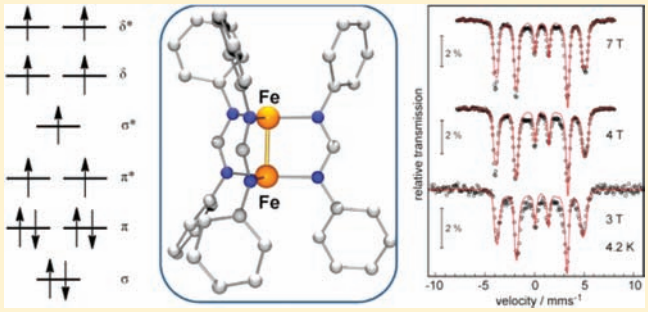

1. INTRODUCTION

Since the seminal discoveries of multiple bonding between transition metal centers in the $[Re_3Cl_{12}]^{3-}$ and $[(ReCl_4)_2]^{2-}$ ions during the 1960s,[1] the study of bimetallic coordination complexes has exposed a rich diversity in the range, nature, physical properties, and reactivity of metal–metal bonds. Continued interest in metal–metal bonds stems from their advantageous properties: the versatility in M–M bonding, the availability of multiple *d*-electrons, and additional coordination sites for substrate binding. These studies are also motivated from a theoretical standpoint: the varied possible orbital interactions between the two metals and the high degree of electron correlation have made for intriguing study and provided challenging tests for current computational methods.[2]

Bimetallic compounds with metal–metal bonds can be catalytically relevant. For example, Rh–Rh bonds play a central role in the dirhodium-catalyzed functionalization of inert C–H bonds.[3] The interesting photochemical properties of Rh–Rh bonds have been utilized in light-to-energy conversion schemes, as for example, in the reduction of protons to hydrogen.[4] Another highlight is the stoichiometric "chop–chop" reaction, wherein multiply bonded ditungsten W≡W compounds undergo metathesis with alkynes (or nitriles) to generate mononuclear tungsten alkylidynes W≡CR (and W≡N).[5] These examples have in common that they feature a second- or third-row transition metal and are diamagnetic. From a practical standpoint, first-row transition metals are ideal because they are inexpensive and earth abundant. Also, in the development of magnetic materials, first-row metal–metal bonds offer more diversity in spin states.[6]

On the theory side, density functional methods have been applied successfully to describe the metal–metal bonds featuring second- and third-row metals,[2a,b] but the extension to first-row metals has been problematic. One vexing issue is electron correlation,[2c] and state-of-the-art quantum chemical methods are often necessary to produce satisfactory descriptions of the metal–metal interaction. A well-studied case is that of multiply bonded Cr_2. We have previously described the bond order in several Cr_2 complexes by using the concept of effective bond order (EBO),[7] which is determined from a multiconfigurational wave function.[8]

Going beyond Cr_2, we are interested in the spectroscopic properties and electronic structures of M–M complexes featuring other first-row transition metals. For iron, complexes with Fe–Fe bonds are well-known, particularly for iron carbonyl clusters and their derivatives. If we exclude compounds with carbonyl ligands, then the number of

Received: November 3, 2011
Published: December 8, 2011

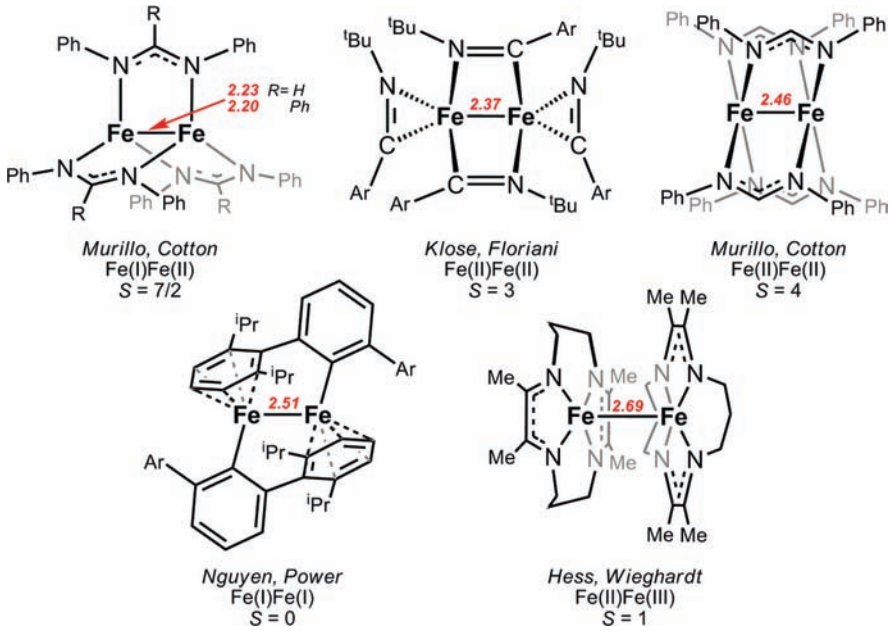

Figure 1. Diiron coordination complexes containing strong Fe−Fe bonds. Relevant characterization data such as Fe−Fe bond lengths (Å), formal oxidation states, and ground spin states are given.

structurally characterized complexes with significant Fe−Fe interactions drastically decreases.[9] Some of these diiron compounds are shown in Figure 1. Collectively, they show great breadth in oxidation states, coordination numbers, geometries, and ligand types.[10] The diiron complex $[Fe_2(C_6H_3\text{-}2,6\text{-}(C_6H_3\text{-}2,6\text{-}^iPr_2)_2)_2]$ has been postulated to be diamagnetic,[10b] although this assignment does not match the $S = 3$ prediction from multiconfigurational quantum chemical calculations.[11] Indeed, the majority of the examples in Figure 1 are paramagnetic with $S \geq 1$, challenging the conventional wisdom that strong metal−metal interactions should be antiferromagnetic.[10a] More remarkable, $Fe_2(DPhF)_3$ and $Fe_2(DPhF)_4$ (DPhF = diphenylforamidinate) both possess high-spin electronic configurations ($S = 7/2$ and 4, respectively), a feat that is unparalleled by other Fe−Fe complexes.[10d,e] A hexairon complex was recently reported with a marvelously high magnetic moment, $S = 6$; but, for six ferrous centers, the analogous "high-spin" configuration would be $S = 12$.[12] To our knowledge, the only other high-spin Fe−Fe species are gas-phase $[Fe_2]^0$ and $[Fe_2]^-$ with $S = 4$ and $S = 7/2$ ground spin-states, respectively.[13] Of note, $Fe_2(DPhF)_3$ is also one of a few examples of a formally mixed-valent Fe(II)Fe(I), although these other complexes are low-spin in contrast to $Fe_2(DPhF)_3$.[14]

In the present work, we examine the nature of the iron−iron bond in $Fe_2(DPhF)_3$, extending the previous studies by Cotton, Murillo et al.[10d,15] Much of the spectroscopic characterization for $Fe_2(DPhF)_3$ is reported for the first time, including Mössbauer, magnetic susceptibility, and UV/visible/near-infrared (UV−vis−NIR) electronic absorption measurements. To complement the physical data, the electronic structure of $Fe_2(DPhF)_3$ has also been calculated by employing a combination of density functional theory (DFT) and multiconfigurational quantum chemical methods. When possible, spectroscopic parameters were calculated, and in general, good agreement was found with experimental values.

2. EXPERIMENTAL SECTION

Synthetic Considerations. All manipulations were performed under a dinitrogen atmosphere in a Vacuum Atmosphere glovebox or using standard Schlenk techniques. Standard solvents were deoxygenated by sparging with dinitrogen and dried by passing through activated alumina columns of a SG Water solvent purification system. Deuterated solvents were purchased from Cambridge Isotope Laboratories, Inc., dried over alumina, filtered, and stored over activated 4 Å molecular sieves.

The synthesis of $Fe_2(DPhF)_3$ is a modified preparation of the literature report,[10d] although it is quite similar to the first reported synthesis.[15] $FeCl_2(HDPhF)_2$ (750 mg, 1.44 mmol) was dissolved in toluene (90 mL) and cooled to −78 °C. *n*-Butyllithium (in hexane, 2.15 mmol) was slowly added dropwise, and the reaction solution was allowed to slowly warm to room temperature over 12 h. The resulting brown mixture was filtered, giving a light yellow−brown solution. After removal of solvent under vacuum, the dried brown solid was redissolved in THF, layered with diethyl ether, and left to crystallize at −35 °C. Yellow crystals of $Fe_2(DPhF)_3$, which formed after 2 days, were filtered and dried under vacuum. Yield: 175 mg, 35%. ^{1}H NMR (500 MHz, THF-d_8, 23 °C): δ = 12.6 (12H, *meta*), −19.6 (6H, *para*), −40 (12H, *ortho*) (see Supporting Information, Figure 1); UV−vis−NIR (THF): λ_{max}, nm (ε, M^{-1} cm^{-1}) = 280 (63000), 350 sh (13000), 650 (50), 700 sh (50), 825 (70), 1250 (80).

X-ray Crystallographic Data Collection and Refinement of the Structures. Single crystals of $Fe_2(DPhF)_3(C_6H_6)_{0.5}$ were grown from vapor diffusion of hexane into a saturated benzene solution of $Fe_2(DPhF)_3$ at room temperature. A thin yellow plate (0.3 mm × 0.3 mm × 0.1 mm) was placed on the tip of a glass capillary and mounted on a Siemens SMART Platform CCD diffractometer for data collection at 173 K. The data collection was carried out using Mo Kα radiation (graphite monochromator). The data intensity was corrected for absorption and decay (SADABS). Final cell constants were obtained from least-squares fits of all measured reflections. The structure was solved using SHELXS-97 and refined using SHELXL-97. A direct-methods solution was calculated which provided most non-hydrogen atoms from the E-map. Full-matrix least-squares/difference Fourier cycles were performed to locate the remaining non-hydrogen atoms. All non-hydrogen atoms were refined with anisotropic displacement parameters. Hydrogen atoms were placed in ideal positions and refined as riding atoms with relative isotropic

dx.doi.org/10.1021/ic202384b | *Inorg. Chem.* 2012, 51, 728−736

displacement parameters. Crystallographic data are summarized in Table 1.

Table 1. Crystallographic Details for $[Fe_2(DPhF)_3](C_6H_6)_{0.5}$

chemical formula	$C_{39}H_{33}N_6Fe_2(C_6H_6)_{0.5}$
formula wt	736.48
cryst syst	triclinic
space group	$P\bar{1}$
a (Å)	11.317(2)
b (Å)	11.954(2)
c (Å)	13.948(2)
α (deg)	108.303(2)
β (deg)	91.290(2)
γ (deg)	95.539(2)
V (Å^3)	1780.4(5)
Z	2
D_{calcd} (g cm^{-3})	1.374
λ (Å), μ (mm^{-1})	0.71073, 0.854
T (K)	173(2)
θ range (deg)	1.54–26.37
reflns collected	7222
unique reflns	4528
data/restraint/parameters	7222/0/451
R_1, wR_2 ($I > 2\sigma(I)$)	0.0599, 0.1056

Physical Measurements. NMR spectra were collected on a Varian Inova 500 MHz spectrophotometer. Room-temperature visible and near-infrared absorption data were collected on a Cary-14 spectrophotometer. UV wavelength absorption spectra were collected on a Cary 300 Bio UV–visible spectrophotometer. Samples of $Fe_2(DPhF)_3$ were recrystallized from THF/hexane prior to data collection, then redissolved in THF (UV, 7.07 μM; Vis–NIR, 6.70 mM).

Magnetic susceptibility data were measured from powder samples of solid material in the temperature range 2 to 300 K by using a SQUID susceptometer with a field of 1.0 T (MPMS-7, Quantum Design, calibrated with standard palladium reference sample, error <2%). Multiple-field variable-temperature magnetization measurements were done at 1 T, 4 T, and 7 T also in the range 2–300 K with the magnetization equidistantly sampled on a $1/T$ temperature scale. The experimental data were corrected for underlying diamagnetism by use of tabulated Pascal's constants[16] as well as for temperature-independent paramagnetism. The susceptibility and magnetization data were simulated with the program julX for exchange-coupled systems.[17] The simulations are based on the usual spin-Hamiltonian operator for mononuclear complexes with spin $S = 7/2$ with consideration of only second-order terms for the zfs:

$$\hat{H} = g\beta\vec{\vec{S}}\cdot\vec{B} + D[\hat{S}_z^2 - 1/3S(S+1) + E/D(\hat{S}_x^2 - \hat{S}_y^2)] \quad (1)$$

where g is the average electronic g value, and D and E/D are the axial zero-field splitting and rhombicity parameters. Magnetic moments are calculated after diagonalization of the Hamiltonian from the eigenfunctions using the Hellman–Feyman theorem $\vec{\mu}_i(\vec{B}) = \langle\psi_i|(dH)/(d\vec{B})|\psi_i\rangle$. Powder summations were done by using a 16-point Lebedev grid.[18] Because the program is not equipped for individual spins larger than 5/2, we reproduced the octet ground state by adopting ferromagnetic coupling of $S_1 = 3/2$ and $S_2 = 2$ with a exceedingly large exchange coupling constant $J = +300$ cm^{-1}. This value is a conservative estimate of the true coupling of the mixed-valence diiron complex because the excited states are higher in energy so that thermal population cannot be detected.

Mössbauer data were recorded on an alternating constant-acceleration spectrometer. The minimum experimental line width was 0.24 mm s^{-1} (full width at half-height). The sample temperature was maintained constant in an Oxford Instruments Variox or an Oxford Instruments Mössbauer-Spectromag 2000 cryostat, which is a split-pair superconducting magnet system for applied fields (up to 8 T). The field at the sample is oriented perpendicular to the γ-beam. The ^{57}Co/Rh source (1.8 GBq) was positioned at room temperature inside the gap of the magnet system at a zero-field position. Isomer shifts are quoted relative to iron metal at 300 K. Magnetic Mössbauer spectra were simulated using the spin-Hamiltonian given in (eq 1). The hyperfine interactions for ^{57}Fe were calculated with the usual nuclear Hamiltonian.[19]

Computational Methods. The $Fe_2(DPhF)_3$ complex was studied using density functional theory (DFT) and the complete active space self-consistent field (CASSCF) method,[8] followed by a multiconfigurational second-order perturbation theory (CASPT2) method.[20] It has been demonstrated that this strategy is successful in predicting accurate results for ground and electronically excited states of bimetallic systems.[21]

DFT Calculations. Geometry optimizations of $Fe_2(DPhF)_3$ were performed for the various possible spin states at the DFT level employing the Perdew–Burke–Ernzerhof (PBE) exchange-correlation functional[22] using the TURBOMOLE 6.1 program package.[23] For all atoms, the double-ζ quality basis sets def-SV(P) were used. DFT calculations were performed with the broken symmetry option (unrestricted calculations) and the resolution-of-the-identity (RI) approximation.[24] Hyperfine parameters were calculated using the ORCA program package.[25] For Fe atoms, the CP(PPP) basis set designed by Neese and co-workers for accurate calculations of hyperfine coupling in transition metal compounds was used.[26] The all-electron Gaussian basis sets used were those reported by Ahlrichs and co-workers, including TZVP basis sets for N atoms and SV(P) for C and H atoms.[27] The DFT calculations of the hyperfine parameters were performed using four functionals B3LYP, BP86, TPSSh, and B2PLYP for comparison.

CASSCF/CASPT2 Calculations. All CASSCF/CASPT2 calculations were performed with the MOLCAS-7.4 package[28] using the DFT-optimized structures with imposed 2-fold symmetry for all possible spin states. The relativistic all-electron ANO-RCC basis sets[29] were used for all elements. Because MOLCAS works in subgroups of D_{2h}, all calculations were performed in the C_2 point group to minimize computational cost. For the Fe and N atoms basis sets of double-ζ quality were used(ANO-RCC-VDZP) with the following contractions: [5s4p2d1f] for Fe and [3s2p1d] for N. The remaining C and H atoms have basis sets of minimal basis quality (ANO-RCC-MB) with a contraction of [2s1p] for C and [1s] for H. Scalar relativistic effects were included by using the Douglas–Kroll–Hess Hamiltonian.[30] The two-electron integral evaluation was simplified by employing the Cholesky decomposition technique.[31]

The ground- and excited-state wave functions were computed at the CASSCF theory level, and corresponding energies were computed at the CASPT2 theory level. An imaginary level shift of 0.2 au was used to avoid intruder states.[32] The natural orbital occupation numbers were used for the evaluation of the effective bond order (EBO),[7a,d] which is calculated as the difference between the total occupancies of the bonding and antibonding molecular orbitals of the Fe–Fe bond divided by two.

CAS Choice. A complete active space was used consisting of all 13 valence electrons of both Fe ions distributed over 13 orbitals, denoted as AS (13, 13). This active space was optimized to include all the 3d Fe orbitals and three additional bonding orbitals, one σ- and two π-(Fe–Fe) MOs that primarily consist of atomic orbitals in the fourth shell of Fe atoms (for correlation effects between the third and fourth shell orbitals of the Fe atoms). Computations of the excited-state wave functions were performed using AS (13, 13) as well as AS (11, 15). The latter active space excludes the lowest doubly occupied σ-orbital formed by the $3d_z^2$-orbitals of Fe ions and includes three additional formally empty MOs of the fourth shell. Many electronic states were computed with the (13, 13) active space, namely the lowest eight octet states belonging to the A irreducible representation, the lowest six octet states belonging to the B irreducible representation, and the lowest six A and B sextet and quartet states. The intensities of the

dx.doi.org/10.1021/ic202384b | Inorg. Chem. 2012, 51, 728–736

Table 2. Selected Bond Lengths (Å) and Angles (deg) for Experimental and Calculated $Fe_2(DPhF)_3$ Structures

structure	$[(DPhF)_3Fe_2]$[10d,15]	$[(DPhF)_3Fe_2]\cdot(C_6H_6)_{0.5}$	$[(DPhF)_3Fe_2]$ *PBE/def-SV(P)*
Fe−Fe, Å	2.2318(8)	2.2307(8)	2.188
Fe−N, Å	2.033(2)	2.032(3)	2.034
	2.033(2)	2.022(3)	2.034
	2.025(2)	2.013(3)	2.034
	2.025(2)	2.005(3)	2.031
	2.017(2)	1.992(3)	2.031
	2.017(2)	1.988(3)	2.031
N−Fe−N, deg	132.6(1)	125.8(1)	121.6
	132.6(1)	125.7(1)	121.6
	116.18(9)	120.5(1)	119.4
	116.18(9)	117.1(1)	119.4
	111.08(9)	116.9(1)	118.7
	111.08(9)	113.7(1)	118.7
N−Fe−Fe, deg	92.29(6)	92.14(9)	92.2
	92.29(6)	91.67(9)	92.2
	90.98(6)	91.39(8)	92.0
	90.98(6)	91.21(8)	92.0
	89.77(7)	90.96(9)	91.8
	89.77(7)	90.15(8)	91.8
N−C−N, deg	122.5(3)	122.5(3)	121.8
	122.5(3)	122.5(3)	121.7
	121.3(3)	122.3(4)	121.7

transitions among all the states including spin−orbit coupling were determined by using the complete active space state interaction method, CASSI,[33] which employs an effective one-electron spin−orbit (SO) Hamiltonian, based on the mean field approximation of the two electronic part.[34] To compute SO coupling, a SO Hamiltonian matrix was constructed using the basis of all 13/13 CASSCF wave functions corresponding to the octet, sextet, and quartet states within 2.2 eV of the ground state. A total of 14 octet, 12 sextet, and 12 quartet states were thus included, giving a total of 232 spin−orbit states. Dynamic correlation energy was introduced in the consideration by substituting the diagonal elements of the Spin−Orbit Hamiltonian matrix by the corresponding CASPT2 energies.

3. RESULTS

Molecular Structure. The published solid-state structure of $Fe_2(DPhF)_3$ shows a distorted trigonal lantern geometry with one of the shortest Fe−Fe bonds, 2.2318(8) Å, known to date (Table 2).[15] A perpendicular C_2 axis bisects the metal−metal bond, symmetrizing the two iron atoms as well as each pair of N atoms. The distortion from idealized D_{3h} is observed in the N−Fe−N bond angles of 111.1°, 116.2°, and 132.6° (Δ = 22°). Cotton and Murillo attributed the distortion to crystal packing forces as opposed to electronic effects. We have obtained another solid-state structure of $Fe_2(DPhF)_3$, in which the Fe−Fe bond is identical to the original report. The only remarkable difference is the tighter range of N−Fe−N bond angles: 113.7−125.8° (Δ = 12°). In the DFT-optimized ground-state structure of $Fe_2(DPhF)_3$ (vide infra), the bond distances match those of the experimental structure within 0.04 Å, including a calculated Fe−Fe bond length of 2.188 Å. Additionally, the N−Fe−N bond angles are nearly equivalent with Δ = 3°. These recent results support the original supposition that acute distortions from C_3 symmetry do not have an electronic basis.

Magnetic Measurements. The ground spin state of $Fe_2(DPhF)_3$ of $S = 7/2$ was previously assigned based on an axial EPR spectrum with g-values of 7.94 and 1.99.[15] Magnetic susceptibility measurements of $Fe_2(DPhF)_3$ have been conducted with variable temperature (VT) and with variable temperature and field (VTVH). The data are shown in Figure 2. From 30 to 290 K, the effective magnetic moment is temperature independent at 7.4 μ_B. The plots in Figure 2 confirm the $S = 7/2$ ground spin state and indicate that the octet state is energetically well-isolated from the other spin

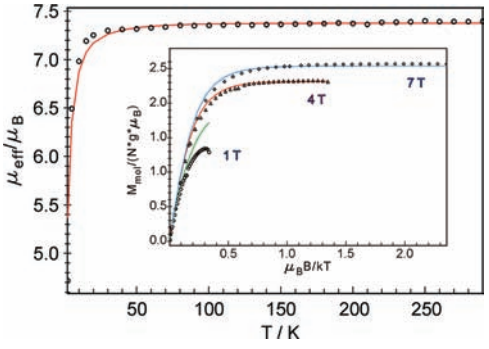

Figure 2. Temperature dependence of the effective magnetic moment, μ_{eff}, of $Fe_2(DPhF)_3$ (shown in open circles, 1 T, 2−290 K). The red solid line represents the best fit. Inset: isofield VTVH magnetization of $Fe_2(DPhF)_3$ as a function of $\mu_B B/kT$ (1, 4, and 7 T; 2−290 K with corresponding simulation curves shown in green, red, and blue, respectively). The data were corrected for χ_{TIP} of 0.375×10^{-3} emu. Intermolecular coupling was considered by introducing a Weiss constant, θ, of −0.286 K to obtain a consistent fit of the low temperature data recorded at different fields. See text for simulation parameters.

dx.doi.org/10.1021/ic202384b | Inorg. Chem. 2012, 51, 728−736

states. To fit the data, we used a two-spin model consisting of the two iron centers, formally high-spin Fe(I) and Fe(II) with S_{Fe} = 3/2 and 2, respectively; otherwise, the iron centers were treated as equivalent. The spectrum can be simulated by adopting g_{Fe} = 1.86, which is near the real value of 2.0 (based on the EPR spectrum), and zero-field splitting parameter D = 19.1 cm^{-1} for both iron centers. The values correspond to a zero-field splitting of the ground state octet according to $D_{7/2}$ = 8.2 cm^{-1}, as can be seen from spin projection coefficient ($D_{7/2}$ = 0.1429 D_1 + 0.2857 D_2).[35] The coupling between the two iron centers is strongly ferromagnetic, with a simulated *minimum* value of the isotropic spin−spin coupling constant J of +300 cm^{-1} for the Hamiltonian $\hat{H} = -2J\hat{S}_{Fe}\bullet\hat{S}_{Fe}$. The inset in Figure 2 shows the VTVH dependence of the magnetization of $Fe_2(DPhF)_3$. The variable field data were globally fitted with the following parameters: g_{Fe} = 1.87, no rhombicity (E/D = 0), and D = +19.1 cm^{-1} for both iron centers. The large, positive zero-field splitting parameter is characteristic of high-spin iron centers and further pinpoints the $m_s = \pm 1/2$ as the ground energy level.

We have performed geometry optimizations for the doublet, quartet, sextet, and octet spin-states using DFT (PBE/def-SV(P)). These optimized structures were then used for higher level CASSCF/CASPT2 calculations, wherein a 2-fold symmetry was imposed to reduce the computational cost. Although $Fe_2(DPhF)_3$ is better suited to 3-fold symmetry, point group constraints in MOLCAS are limited to D_{2h} and its subgroups. Therefore, we chose to impose C_2 symmetry, which enforces a 2-fold rotation axis perpendicular to the Fe−Fe vector. The relative energies for the various states calculated at these three levels of theory are reported in Table 3. All methods

Table 3. Calculated Relative Energies of $Fe_2(DPhF)_3$ for All Possible Spin States at DFT, CASSCF, and CASPT2 Levels of Theory

	symmetry	doublet	quartet	sextet	octet
ΔE_{DFT}, eV	—	2.95	1.65	0.71	0
ΔE_{CASSCF}, eV	*A*	1.63	1.10	1.30	0
	B	1.44	1.44	0.60	1.26
ΔE_{CASPT2}, eV	*A*	1.50	1.22	1.17	0
	B	1.53	1.22	0.50	1.18

indicate that the ground state is the octet ^{8}A, as previously proposed.[36] Selected geometrical parameters of the structure of the ^{8}A state are reported in Table 2. Overall, the agreement between theory and experiment is satisfactory.

Mössbauer Spectroscopy. Applied-field Mössbauer spectra of $Fe_2(DPhF)_3$ recorded at 4.2 K are shown in Figure 3. Additional spectra collected at variable temperatures are provided in the Supporting Information (Figure 2). The spectra were globally fitted with an isotropic $g_{7/2}$ = 2.0, $D_{7/2}$ = 8.2 cm^{-1}, $E/D_{7/2}$ = 0, and the Mössbauer parameters δ = 0.65 mm s^{-1} and ΔE_Q = +0.32 mm s^{-1}. On the basis of the fit, we can draw some conclusions. First, the g, D, and E/D values correspond well to those obtained in the magnetic susceptibility measurements. Second, the two iron sites are equivalent on the Mössbauer time scale (10^7 s^{-1}), and $Fe_2(DPhF)_3$ is a fully delocalized mixed-valent complex. The quantum-chemical treatment given below will show that the diiron core of the

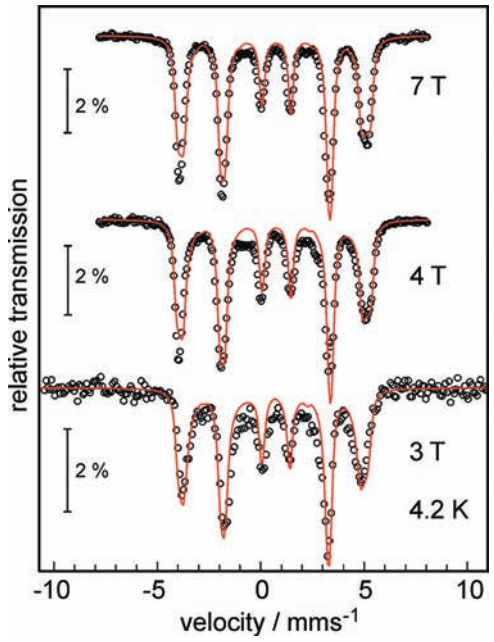

Figure 3. Applied field Mössbauer spectra of $Fe_2(DPhF)_3$ recorded at 4.2 K with fields of 3, 4, and 7 T. The solid lines represent spin Hamiltonian simulations for S = 7/2 with $g_{7/2}$ = (2.0, 2.0, 2.0) fixed, $D_{7/2}$ = 8.2 cm^{-1}, and $E/D_{7/2}$ = 0, and with Mössbauer parameters δ = 0.65 mm s^{-1}, ΔE_Q = +0.32 mm s^{-1}, asymmetry parameter η = 0, line width = 0.26 mm s^{-1}, and magnetic hyperfine coupling constants $A_{xx}/g_N\beta_N$ = −11.59 T; $A_{yy}/g_N\beta_N$ = −10.59; $A_{zz}/g_N\beta_N$ = −30.81 T. The spin projection coefficients in the ionic limit of Fe(I), S_1 = 3/2, and Fe(II), S_2 = 2 would be $A_{Fe(I)} = 2.333 \cdot A$, and $A_{Fe(II)} = 1.751 \cdot A$, respectively, i.e., the local A values for the iron sites are about twice the total spin values given here.

compound is best described by a coherent superposition of Fe(I) and Fe(II) wave functions.

There are limited examples of low-coordinate, high-spin Fe(II) and Fe(I) complexes for comparison. Holland et al. have reported Mössbauer parameters for a family of three-coordinate, high spin Fe(II) compounds with β-diketiminate ligands.[37] The isomer shifts range from 0.48 to 0.74 mm s^{-1} with $|\Delta E_Q|$ values between 1.11 and 1.74 mm s^{-1}. For a high-spin Fe(I) complex in the same system, a slightly lower isomer shift of 0.44 mm s^{-1} with ΔE_Q = 2.02 mm s^{-1} was reported.[38] Peters et al. have characterized a Fe(I)(μ-N_2)Fe(I) complex with δ = 0.53 mm s^{-1} and ΔE_Q = +0.89 mm s^{-1}.[39] The isomer shift reported here is comparable. Notably, the quadrupole splitting of $Fe_2(DPhF)_3$ is significantly smaller. The origin of the small quadrupole interaction is not known at this time, but it may be potentially related to the weak trigonal ligand field.

The Mössbauer parameters were calculated at the DFT level of theory using the ORCA program (Table 4).[25] Four different functionals were surveyed: B2PLYP, BP86, TPSSh, and

Table 4. Calculated Hyperfine Parameters of $Fe_2(DPhF)_3$ Relevant to Mössbauer Spectroscopy for Different DFT Functionals (B2PLYP, BP86, TPSSh, B3LYP)

functional	exp	B2PLYP[a]	BP86[a]	TPSSh[a]	B3LYP[a]	B3LYP[b]
δ, mm/s	0.65	0.49	0.45	0.48	0.49	0.51
ΔE_Q, mm/s	0.32	0.26	−0.45	−0.17	−0.27	−0.25

[a]Input geometry from a PBE/SV(P) optimization. [b]Input geometry from a B3LYP/TZV(P) optimization.

dx.doi.org/10.1021/ic202384b | Inorg. Chem. 2012, 51, 728−736

B3LYP.[26b,40] For the isomer shift, all the functionals gave similar predictions (within 0.20 mm s^{-1} of the experimental value). Although the range of quadrupole splittings is wider (from −0.17 to 0.26 mm s^{-1}), essentially all these values are near zero, as is observed experimentally. The best agreement between theory and experiment was found for the B2PLYP functional with δ = 0.49 mm s^{-1} and ΔE_Q = 0.26 mm s^{-1}, where Δ = 0.16 and 0.06 mm s^{-1}, respectively.

Details of Electronic Structure. The natural orbitals arising from the CASSCF calculations are displayed in Figure 4. Ten of the 13 orbitals are completely localized on the Fe−Fe

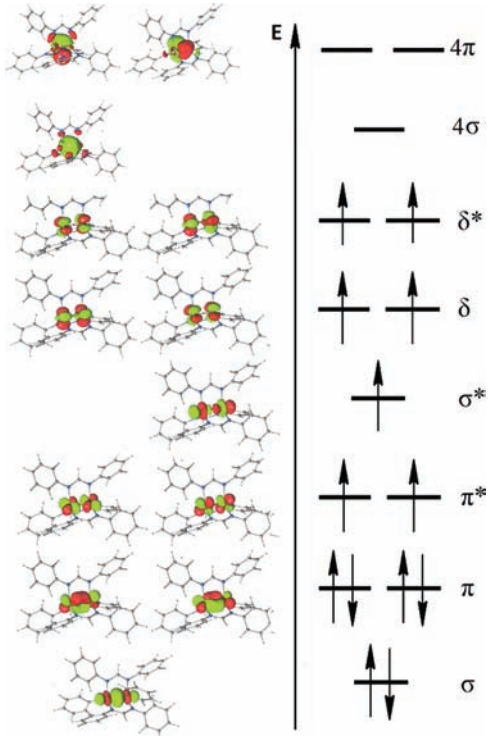

Figure 4. Qualitative MO diagram showing the natural orbitals for $Fe_2(DPhF)_3$ that arise from CASSCF calculations. The dominating electronic configuration (73%) is shown.

bond. They are the σ, π, and δ bonding and antibonding orbitals, resulting from symmetry-adapted linear combinations of the Fe 3*d* atomic orbitals. The three remaining orbitals are primarily composed of the Fe 4*s*, 4*p*, and 4*d* atomic orbitals interacting to form σ and π bonding and antibonding orbitals with some minor contribution from the ligand N-atoms. The near degeneracy of each π- and δ-orbital pair is consistent with an approximate 3-fold symmetry about the Fe−Fe vector.

A multiconfigurational CASSCF/CASPT2 calculation revealed that the ^8A ground state has a single dominating configuration $(\sigma)^2(\pi)^4(\pi^*)^2(\sigma^*)^1(\delta)^2(\delta^*)^2$, which accounts for 73% of the wave function. Considering the total ground-state wave function, the natural orbital occupation numbers are: $(\sigma)^{1.85}(\pi)^{3.64}(\pi^*)^{2.30}(\sigma^*)^{1.06}(\delta)^{2.00}(\delta^*)^{2.00}(4\sigma)^{0.10}(4\pi)^{0.06}$ with an estimated bond order (EBO) of 1.15. The non-negligible occupation of the iron orbitals in the fourth shell is also evident in the Mulliken population analysis: $4s^{0.12}3d^{6.32}4p^{0.28}4d^{0.11}$. Using an SCF-X$\alpha$-SW calculation on the truncated molecule $Fe_2(HNCHNH)_3$, Cotton et al. previously computed a similar configuration $(\sigma)^2(\pi)^4(\pi^*)^2(\delta)^2(\sigma^*)^1(\delta^*)^2$ with a bond order of 1.5.[36] It is not surprising that our EBO value is lower than the value reported by Cotton because we account for the partial occupation of the high-lying antibonding orbitals not represented in the dominant configuration. Overall, the effect is to decrease the Fe−Fe bonding so that it is only slightly larger than a single bond. Finally, the charge and spin densities of the two iron atoms are identical with values of +1.17 and +3.49, respectively. These values reinforce the highly delocalized, high-spin $Fe^{1.5}Fe^{1.5}$ assignment for the diiron unit.

Electronic Absorption Spectroscopy. The electronic configuration in Figure 4 suggests that several *d*−*d* transitions are possible within the diiron core. Because the first coordination sphere of the diiron centers is approximately 3-fold symmetric, we first employed D_{3h} selection rules to qualitatively determine the allowed electric-dipole transitions (Figure 5). Electronic transitions from the $^8A_2''$ ground-state are spin-allowed only if the excited electron is spin down, which

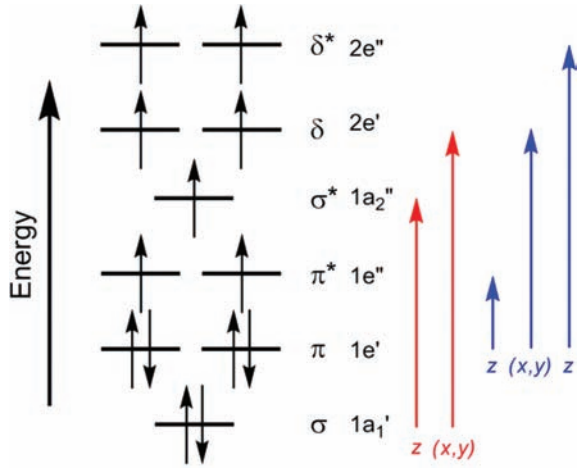

Figure 5. The allowed electric-dipole transitions of $Fe_2(DPhF)_3$ based on D_{3h} selection rules.

constrains all transitions to originate from a doubly occupied molecular orbital such as $1a_1''(\sigma)$ or $1e'(\pi)$. Within the *d*-orbital manifold, only five electric-dipole transitions are possible, from $1a_1''(\sigma)$ to $1a_2''(\sigma^*)$ or $2e'(\delta)$, and from $1e'(\pi)$ to $1e''(\pi^*)$, $2e'(\delta)$, or $2e''(\delta^*)$. Of these five transitions, the energetically lowest transition is expected to be $1e'(\pi) \rightarrow 1e''(\pi^*)$.

The Vis−NIR spectrum for $Fe_2(DPhF)_3$, which is shown in Figure 6, is characterized by several low energy bands between 650 and 1250 nm (15400 and 8000 cm^{-1}). The Vis−NIR absorptions are independent of solvent as identical spectra are obtained in benzene and in THF (Supporting Information, Figure 3). These bands are surprisingly weak (ε < 100 M^{-1} cm^{-1}) given the expectation that they should be both spin- and dipole-allowed. Indeed, metal−metal intervalence charge transfer bands exhibited by delocalized, mixed-valent bimetallics are typically intense ($\varepsilon \sim 10^3$ M^{-1} cm^{-1}). One possible explanation for the observed weak absorptions is the significance of the Franck−Condon factor in modulating their intensity. Because the Fe−Fe bond distances in the $Fe_2(DPhF)_3$ excited states are expected to be perturbed from their ground-state values, it is plausible that the overlap of vibrational wave functions in the ground and excited electronic states is significantly decreased.

Computed Spin-Free Excited State Energies. As mentioned above, all CASSCF/CASPT2 calculations were performed with a C_2 symmetry constraint that corresponds to a 2-fold axis perpendicular to the internuclear axis. In the following

dx.doi.org/10.1021/ic202384b | *Inorg. Chem.* 2012, 51, 728−736

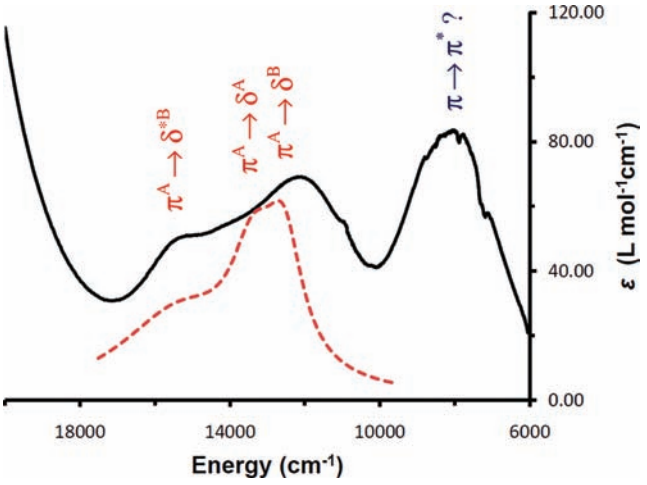

Figure 6. Electronic absorption spectrum of $Fe_2(DPhF)_3$ in THF (—, black), with simulated spectrum from CASSCF/CASPT2 calculations (---, red) that include wave functions belonging to both *A* and *B* symmetry states (see Table 6). Experimental λ_{max}, cm^{-1} (ε, L mol^{-1} cm^{-1}) = 15380 (50), 14290 sh (50), 12120 (70), 8000 (80).

discussion, all wave functions will belong either to the *A* or *B* symmetry states. Table 5 shows the vertical excitation energies and oscillator strengths for $Fe_2(DPhF)_3$ calculated at the spin-free CASSCF and CASPT2 levels using the (13, 13) active space, where the weight is the percent contribution of the major configuration in the excited wave function. All the octet excited states are reported up to 3.11 eV. Only one of the first eight predicted transitions (Table 5, in boldface) has an oscillator strength of any significance: the $\pi \rightarrow \delta$ transition is predicted to occur at 1.66 eV (~13400 cm^{-1}) at the CASPT2 level with an oscillator strength of 2.56×10^{-4}. Of note, the large differences in ΔE (~1 eV) between $\pi \rightarrow \delta$ and $\sigma \rightarrow \delta$ transitions suggest that the σ orbital lies significantly lower in energy. Consequently, transitions originating from the σ orbital do not contribute to the bands in the Vis–NIR region.

Table 5. Spin-Free Excitation Energies of $Fe_2(DPhF)_3$ for Octet Wave Functions Belonging to the *A* Symmetry States (All Transitions Correspond to $^8A \rightarrow {}^8A$)

	ΔE, eV			
transition	(CASSCF)	(CASPT2)	oscillator strength, a.u.	weight, %[a]
$\pi \rightarrow \pi^*$	1.23	1.42	0.235×10^{-7}	0.64
$\pi \rightarrow \pi^*$	1.28	1.45	$<0.1 \times 10^{-7}$	0.63
$\pi \rightarrow \delta$	1.77	1.60	0.788×10^{-5}	0.54
$\pi \rightarrow \delta$	**1.82**	**1.66**	**0.256×10^{-3}**	**0.53**
$\pi \rightarrow \sigma^*$	1.98	1.92	$<0.1 \times 10^{-7}$	0.51
$\pi \rightarrow \delta^*$	2.07	2.06	0.777×10^{-7}	0.27
$\pi \rightarrow \delta^*$	2.24	2.13	0.118×10^{-6}	0.34
$\sigma \rightarrow \delta$	2.79	2.51	0.827×10^{-4}	0.67

[a]Weight is the percent contribution of the major configuration to the wave function describing the excited state.

Given the poor correspondence between theory and experimental excitation energies thus far, our next attempt to model the electronic spectrum included excited states belonging to both symmetry states *A* and *B*. Only the transitions with significant oscillator strengths are shown in Table 6. The consideration of these additional wave functions resulted in two additional excitations.

Hence, three significant excited energies are predicted at 1.56, 1.66 and 1.91 eV, and they are interpreted as $\pi^A \rightarrow \delta^B$, $\pi^A \rightarrow \delta^A$, and $\pi^A \rightarrow \delta^{*B}$ transitions, respectively. Moreover, these computed energies agree well with the experimental spectrum from 18000 to 10000 cm^{-1}. The NIR band at 1250 nm (0.99 eV or 8000 cm^{-1}), however, remains unaccounted, prompting further investigation.

Table 6. Selected Spin-Free Excitation Energies of $Fe_2(DPhF)_3$ for Octet Wave Functions Belonging to the *A* and *B* Symmetry States (All Transitions Correspond to $^8A \rightarrow {}^8A$ or $^8A \rightarrow {}^8B$)

molecular orbital	state transition	ΔE, eV (cm^{-1}, rounded)	oscillator strength, a.u.	weight, %[a]
$\pi^A \rightarrow \delta^A$	$^8A \rightarrow {}^8A$	1.66 (13,400)	0.14×10^{-3}	54
$\pi^A \rightarrow \delta^B$	$^8A \rightarrow {}^8B$	1.56 (12,560)	0.13×10^{-3}	45
$\pi^A \rightarrow \delta^{*B}$	$^8A \rightarrow {}^8B$	1.91 (15,370)	0.29×10^{-3}	24

[a]Weight is the percent contribution of the major configuration to the wave function describing the excited state.

The Nature of the NIR Band at 8000 cm^{-1}. To better model the full Vis–NIR spectrum of $Fe_2(DPhF)_3$, spin–orbit coupling was taken into consideration. The most important excited energies correspond to transitions from pure (>99%) octet ground states (A) to octet-dominated excited states (84–97%) with limited mixing of the sextet configurations. Details of the prominent excited energies are available in the Supporting Information, Table 1. Because of the limited mixing, the calculated excited energies with spin–orbit coupling are essentially identical to those obtained from the spin-free calculations. Therefore, the NIR band at 8000 cm^{-1} is not reproduced by considering spin–orbit coupling.

Another strategy is to increase the active space. An attempt to increase the active space with three additional high-lying MOs, however, was unstable. A stable active space was eventually formed by adding three high-lying MOs while removing the energetically low-lying, doubly occupied σ MO to generate an (11, 15) configuration. The vertical excited energies now include a low energy absorption at 0.80 eV (~6500 cm^{-1}), which is interpreted as $\pi \rightarrow \pi^*$ transition. Although this excited energy corresponds well to the NIR band, the $\pi \rightarrow \delta/\delta^*$ transition energies shift to lower energies of ~1.00 eV and, consequently, worsens the holistic fit. Ideally, employing an even larger active space should result in more accurate excitation energies, but such calculations are currently too expensive. We tentatively interpret the NIR band as a $\pi \rightarrow \pi^*$ transition.

3. CONCLUSIONS

The nature of the Fe–Fe bond in $Fe_2(DPhF)_3$ is strongly ferromagnetic, which essentially arises from the presence of a series of close lying nonbonding and antibonding metal–metal orbitals that are populated according to Hund's rule. Because this type of metal–metal bond is so rare, our study is only one of a few in-depth case studies of strong ferromagnetic interactions via metal–metal bonds.[12,41] Because of the high-spin electronic structure of the $[Fe_2]^{3+}$ unit, the estimated Fe–Fe bond order is low at 1.15, in spite of the relatively short Fe–Fe bond length. The MO analysis reveals that all *d*-electrons are involved in metal–metal σ/σ^*, π/π^*, and δ/δ^* bonds. Though the octet ground spin state is dominant above room temperature, *d*–*d* transitions occur from the π to the π^*, δ,

dx.doi.org/10.1021/ic202384b | Inorg. Chem. 2012, 51, 728–736

and δ^* orbitals in the visible and near-infrared regions. Surprisingly, these $d-d$ transitions are remarkably weak in intensity and hence appear to be forbidden, even though the analysis shows that they are indeed both spin- and dipole-allowed. The electronic structure of the mixed-valent diiron complex is highly delocalized, and the two iron centers are spectroscopically equivalent. Perhaps these will prove to be common features among bimetallics with strong ferromagnetic metal−metal bonds as more examples emerge. Future work will also focus on studying the reactivity of these strongly ferromagnetic metal−metal bonds.[42]

■ ASSOCIATED CONTENT

Ⓢ Supporting Information

Additional spectroscopic characterization and computational details for $Fe_2(DPhF)_3$ (PDF, CIF). This material is available free of charge via the Internet at http://pubs.acs.org.

■ AUTHOR INFORMATION

Corresponding Author

*E-mail: bill@mpi-muelheim.mpg.de (E.B.); gagliard@umn.edu (L.G.); clu@umn.edu (C.C.L.).

Author Contributions

[§]These authors contributed equally.

■ ACKNOWLEDGMENTS

ConocoPhillips is gratefully acknowledged for providing a graduate fellowship to C.M.Z. X-ray diffraction studies were performed at the X-ray Crystallographic Laboratory in the Department of Chemistry (UM) directed by Dr. Victor Young, Jr. Computing support and resources were provided by the Minnesota Supercomputing Institute, and funding for this work was provided by the University of Minnesota. C.C.L. thanks Prof. Karl Wieghardt, Prof. Ted Betley (Harvard University), and Prof. John Berry (University of Wisconsin—Madison) for sharing their thoughts on metal−metal interactions.

■ REFERENCES

(1) Cotton, F. A., Metal-Metal Multiple Bonds and Metal Clusters. In *Reactivity of Metal−Metal Bonds*, Chisholm, M. H., Ed. American Chemical Society: Washington, D. C., 1981; Vol. *155*, pp 1−16.

(2) (a) Cotton, F. A.; Feng, X. *J. Am. Chem. Soc.* **1998**, *120*, 3387−3397. (b) Cotton, F. A.; Feng, X. *J. Am. Chem. Soc.* **1997**, *119*, 7514−7520. (c) Hall, M. B. *Polyhedron* **1987**, *6*, 679−684. (d) Petrie, S.; Stranger, R. *Inorg. Chem.* **2004**, *43*, 2597−2610.

(3) (a) Timmons, D. J.; Doyle, M. P., Chiral Dirhodium(II) Catalysts and Their Applications. In *Multiple Bonds Between Metal Atoms*, 3rd ed.; Cotton, F. A., Murillo, C. A., Walton, R. A., Eds.; Springer Science: New York, 2005; pp 591−632. (b) Davies, H. M. L.; Beckwith, R. E. J. *Chem. Rev.* **2003**, *103*, 2861−2903. (c) Doyle, M. P.; Ren, T. *Prog. Inorg. Chem.* **2001**, *49*, 113−168.

(4) (a) Dempsey, J. L.; Esswein, A. J.; Manke, D. R.; Rosenthal, J.; Soper, J. D.; Nocera, D. G. *Inorg. Chem.* **2005**, *44*, 6879−6892. (b) Heyduk, A. F.; Macintosh, A. M.; Nocera, D. G. *J. Am. Chem. Soc.* **1999**, *121*, 5023−5032. (c) Heyduk, A. F.; Nocera, D. G. *Science* **2001**, *293*, 1639−1641.

(5) (a) Schrock, R. R.; Listemann, M. L.; Sturgeoff, L. G. *J. Am. Chem. Soc.* **1982**, *104*, 4291−4293. (b) Strutz, H.; Schrock, R. R. *Organometallics* **1984**, *3*, 1600−1601. (c) Chisholm, M. H.; Davidson, E. R.; Pink, M.; Quinlan, K. B. *Chem. Commun.* **2002**, 2770−2771.

(6) Metal−metal multiply bonded complexes of second-row transition metals are not all low spin. A general exception are the $[Ru_2]^{5+}$ cores, which are intermediate spin $S = 3/2$. See Angaridis, P. Ruthenium Compounds. In *Multiple Bonds Between Metal Atoms*, 3rd ed.; Cotton, F. A., Murillo, C. A., Walton, R. A., Eds.; Springer Science: New York, 2005; pp 377−430.

(7) (a) Roos, B. O.; Borin, A. C.; Gagliardi, L. *Angew. Chem., Int. Ed.* **2007**, *46*, 1469−1472. (b) La Macchia, G.; Li Manni, G.; Todorova, T. K.; Brynda, M.; Aquilante, F..; Roos, B. O.; Gagliardi, L. *Inorg. Chem.* **2010**, *49*, 5216−5222. (c) La Macchia, G.; Veryazov, V.; Roos, B. O.; Gagliardi, L. *Inorg. Chem.* **2008**, *47*, 11455−11457. (d) Brynda, M.; Gagliardi, L.; Roos, B. O. *Chem. Phys. Lett.* **2009**, *471*, 1−10.

(8) Roos, B. O.; Taylor, P. R.; Siegbahn, P. E. M. *Chem. Phys.* **1980**, *48*, 157−173.

(9) Allen, F. *Acta Crystallogr., Sect. B: Struct. Sci.* **2002**, *58*, 380−388.

(10) (a) Hess, C. R.; Weyhermüller, T.; Bill, E.; Wieghardt, K. *Angew. Chem., Int. Ed.* **2009**, *48*, 3703−3706. (b) Nguyen, T.; Merrill, W. A.; Ni, C.; Lei, H.; Fettinger, J. C.; Ellis, B. D.; Long, G. J.; Brynda, M.; Power, P. P. *Angew. Chem., Int. Ed.* **2008**, *47*, 9115−9117. (c) Klose, A.; Solari, E.; Floriani, C.; Chiesi-Villa, A.; Rizzoli, C.; Re, N. *J. Am. Chem. Soc.* **1994**, *116*, 9123−9135. (d) Cotton, F. A.; Daniels, L. M.; Falvello, L. R.; Matonic, J. H.; Murillo, C. A. *Inorg. Chim. Acta* **1997**, *256*, 269−275. (e) Cotton, F. A.; Daniels, L. M.; Matonic, J. H.; Murillo, C. A. *Inorg. Chim. Acta* **1997**, *256*, 277−282.

(11) La Macchia, G.; Gagliardi, L.; Power, P. P.; Brynda, M. *J. Am. Chem. Soc.* **2008**, *130*, 5104−5114.

(12) Zhao, Q.; Harris, T. D.; Betley, T. A. *J. Am. Chem. Soc.* **2011**, *133*, 8293−8306.

(13) (a) Leopold, D. G.; Almlöf, J.; Lineberger, W. C.; Taylor, P. R. *J. Chem. Phys.* **1988**, *88*, 3780−3783. (b) Hübner, O.; Sauer, J. *Chem. Phys. Lett.* **2002**, *358*, 442−448.

(14) (a) Liu, T.; Darensbourg, M. Y. *J. Am. Chem. Soc.* **2007**, *129*, 7008−7009. (b) Justice, A. K.; Nilges, M. J.; Rauchfuss, T. B.; Wilson, S. R.; De Gioia, L.; Zampella, G. *J. Am. Chem. Soc.* **2008**, *130*, 5293−5301. (c) Justice, A. K.; Rauchfuss, T. B.; Wilson, S. R. *Angew. Chem., Int. Ed.* **2007**, *46*, 6152−6154. (d) Thomas, C. M.; Darensbourg, M. Y.; Hall, M. B. *J. Inorg. Biochem.* **2007**, *101*, 1752−1757.

(15) Cotton, F. A.; Daniels, L. M.; Falvello, L. R.; Murillo, C. A. *Inorg. Chim. Acta* **1994**, *219*, 7−10.

(16) (a) O'Connor, C. J. Magnetochemistry—Advances in Theory and Experimentation. In *Prog. Inorg. Chem.*, Lippard, S. J., Ed.; John Wiley & Sons, Inc.: New York, 1982; Vol. *29*, pp 203−283. (b) Weast, R. C.; Astle, M. J. *CRC Handbook of Chemistry and Physics*; CRC Press Inc.: Boca Raton, FL, 1979.

(17) Bill, E. *julX version 141*; available from: http://ewww.mpi-muelheim.mpg.de/bac/logins/bill/julX_en.php.

(18) Lebedev, V. I.; Laikov, D. N. *Dokl. Math.* **1999**, *59*, 477−481.

(19) Trautwein, A. X.; Bill, E.; Bominaar, E. L.; Winkler, H. *Struct. Bonding (Berlin)* **1991**, *78*, 1−95.

(20) Andersson, K.; Malmqvist, P.-Å.; Roos, B. O. *J. Chem. Phys.* **1992**, *96*, 1218−1226.

(21) (a) Gagliardi, L.; Roos, B. O. *Inorg. Chem.* **2003**, *42*, 1599−1603. (b) Ferrante, F.; Gagliardi, L.; Bursten, B. E.; Sattelberger, A. P. *Inorg. Chem.* **2005**, *44*, 8476−8480. (c) Poineau, F.; Forster, P. M.; Todorova, T. K.; Gagliardi, L.; Sattelberger, A. P.; Czerwinski, K. R. *Inorg. Chem.* **2010**, *49*, 6646−6654. (d) Poineau, F.; Gagliardi, L.; Forster, P. M.; Sattelberger, A. P.; Czerwinski, K. R. *Dalton Trans.* **2009**, 5954−5959. (e) Briggs, B. N.; McMillin, D. R.; Todorova, T. K.; Gagliardi, L.; Poineau, F.; Czerwinski, K. R.; Sattelberger, A. P. *Dalton Trans.* **2010**, *39*, 11322−11324.

(22) Perdew, J. P.; Zunger, A. *Phys. Rev. B* **1981**, *23*, 5048−5079.

(23) *TURBOMOLE V6.1 2010*; University of Karlsruhe and Forschungszentrum Karlsruhe GmbH: Karlsruhe, 1989−2007; TURBOMOLE GmbH: Karlsruhe, 2007; available from http://www.turbomole.com.

(24) Ahlrichs, R.; Bar, M.; Haser, M.; Horn, H.; Kolmel, C. *Chem. Phys. Lett.* **1989**, *162*, 165−169.

(25) Neese, F. *ORCA version 2.8−20*; available from http://www.thch.uni-bonn.de/tc/orca/.

(26) (a) Neese, F. *Inorg. Chim. Acta* **2002**, *337*, 181−192. (b) Sinnecker, S.; Slep, L. D.; Bill, E.; Neese, F. *Inorg. Chem.* **2005**, *44*, 2245−2254.

(27) (a) Schäfer, A.; Horn, H.; Ahlrichs, R. *J. Chem. Phys.* **1992**, *97*, 2571−2577. (b) Schäfer, A.; Huber, C.; Ahlrichs, R. *J. Chem. Phys.* **1994**, *100* (8), 5829−5835.
(28) Aquilante, F.; De Vico, L.; Ferré, N.; Ghigo, G.; Malmqvist, P.-Å.; Pedersen, T.; Pitonak, M.; Reiher, M.; Roos, B. O.; Serrano-Andrés, L.; Urban, M.; Veryazov, V.; Lindh, R. *J. Comput. Chem.* **2010**, *31*, 224−247.
(29) (a) Roos, B. O.; Lindh, R.; Malmqvist, P. A.; Veryazov, V.; Widmark, P. O. *J. Phys. Chem. A* **2004**, *108*, 2851−2858. (b) Roos, B. O.; Lindh, R.; Malmqvist, P. A.; Veryazov, V.; Widmark, P. O. *J. Phys. Chem. A* **2005**, *109*, 6575−6579.
(30) Hess, B. A. *Phys. Rev. A* **1986**, *33*, 3742−3748.
(31) (a) Aquilante, F.; Pedersen, T. B.; Lindh, R. *J. Chem. Phys.* **2007**, *126*, 194106−194111. (b) Aquilante, F.; Pedersen, T. B.; Lindh, R.; Roos, B. O.; De Meras, A. S.; Koch, H. *J. Chem. Phys.* **2008**, *129*, 24113−24118. (c) Aquilante, F.; Malmqvist, P.-A.; Pedersen, T. B.; Ghosh, A.; Roos, B. O. *J. Chem. Theory Comp.* **2008**, *4*, 694−702.
(32) Forsberg, N.; Malmqvist, P.-Å. *Chem. Phys. Lett.* **1997**, *274*, 196−204.
(33) Malmqvist, P. Å. *Int. J. Quantum Chem.* **1986**, *30*, 479−494.
(34) Roos, B. O.; Malmqvist, P.-A. *Phys. Chem. Chem. Phys.* **2004**, *6*, 2919−2927.
(35) Bencini, A.; Gatteschi, D., *Electron Paramagnetic Resonance of Exchange Coupled Systems*; Springer Verlag: Berlin, 1990.
(36) Cotton, F. A.; Feng, X.; Murillo, C. A. *Inorg. Chim. Acta* **1997**, *256*, 303−308.
(37) Andres, H.; Bominaar, E. L.; Smith, J. M.; Eckert, N. A.; Holland, P. L.; Münck, E. *J. Am. Chem. Soc.* **2002**, *124*, 3012−3025.
(38) Stoian, S. A.; Yu, Y.; Smith, J. M.; Holland, P. L.; Bominaar, E. L.; Münck, E. *Inorg. Chem.* **2005**, *44*, 4915−4922.
(39) Hendrich, M. P.; Gunderson, W.; Behan, R. K.; Green, M. T.; Mehn, M. P.; Betley, T. A.; Lu, C. C.; Peters, J. C. *Proc. Natl. Acad. Sci. U.S.A.* **2006**, *103*, 17107−17112.
(40) Römelt, M.; Ye, S.; Neese, F. *Inorg. Chem.* **2009**, *48*, 784−785.
(41) Timmer, G. H.; Berry, J. F. *C. R. Chim.* **2011**, DOI: 10.1016/j.crci.2011.09.001.
(42) (a) Powers, T. M.; Fout, A. R.; Zheng, S.-L.; Betley, T. A. *J. Am. Chem. Soc.* **2011**, *133*, 3336−3338. (b) Harris, T. D.; Betley, T. A. *J. Am. Chem. Soc.* **2011**, *133*, 13852−13855.